ANALYTICAL SOLUTION OF A DISSIPATIVE FLOW CONVEYING TERNARY HYBRID NANOFLUIDS INDUCED BY A POROUS SURFACE WITH LORENTZ FORCES

Ibrahim MAHARIQ[*/**/***], **Mohamed KEZZAR**[****], **Pachiyappan RAGUPATHI**[*****], **Umair KHAN**[******/*******], **Farhan Lafta RASHID**[********], **Abeer SHAABAN**[*********], **Mohamed Rafik SARI**[**********]

[*]College of Engineering and Architecture, Gulf University for Science and Technology, Mishref, Kuwait
**University College, Korea University, Seoul 02481, South Korea
***Najjad Zeenni Faculty of Engineering, Al-Quds University, Jerusalem, Palestine
****Materials and Energy Engineering Laboratory (LMGE), Technology Department, Faculty of Technology, 21000 Skikda, Algeria
*****Department of Mathematics, Sri Ramakrishna Mission Vidyalaya College of Arts and Science, Coimbatore 641020, India
******Department of Mathematics, Saveetha School of Engineering, Saveetha Institute of Medical and Technical Sciences, Saveetha University, Chennai 602105, Tamil Nadu, India
*******Department of Mathematics, Faculty of Science, Sakarya University, Serdivan/Sakarya 54050, Turkey
********Petroleum Engineering Department, College of Engineering, University of Kerbala, Karbala 56001, Iraq
*********Department of Management Information of Business and Economics, Qassim University, Buraydah, Saudi Arabia
**********Mechanics of Materials and Plant Maintenance Research Laboratory (LR3MI), Mechanical Engineering Department, Faculty of Technology, Badji Mokhtar- Annaba University, Annaba, 23000, Algeria

ibmahariq@gmail.com, kezzar_m@yahoo.com, ragupathiprs@gmail.com, umairkhan@sakarya.edu.tr, farhan.lefta@uokerbala.edu.iq, a.shaban@qu.edu.sa, mohamed-rafik.sari@univ-annaba.dz

received 15 February 2025, revised 12 May 2025, accepted 10 June 2025

Abstract: The study presents a mathematical model to predict the impact of interfacial nanolayers on mass and heat transfer phenomena in ternary hybrid nanofluid (THNF) flow. It also investigates the effect of TiO_2, SiO_2 and Al_2O_3 in non-Newtonian biological fluids (i.e. blood) using porous surfaces. The study includes uniform transverse magnetic flux (MF) and reduces the nonlinear partial differential equations (PDEs) to ordinary differential equations (ODEs) using similarity transformations then solved analytically and numerically, the analytical method has been established using the Adomian Decomposition Method (ADM) and by the numerical procedure (Explicit Runge Kutta Method), the present findings in specified cases are compared to findings obtained by the Homotopy Analysis Method (HAM)-based Mathematica package and by the previous literature for validation. The research focused on the influence of active parameters on various parameters, numerically and graphically examining their impact. Results show that the velocity profile experienced a 20% enhancement in the channel centerline region when using a 0.5 unsteadiness parameter (α) together with M = 1 as the magnetic parameter value. This enhancement was possible through the 15% reduction in momentum boundary layer thickness. The heat transfer capabilities of ternary hybrid nanofluids containing 2% nanoparticle volume fractions boost the performance by 25% better than pure base fluids.

Keywords: nanolayers, ternary hybrid nanofluid, non-Newtonian, biological fluids, ADM and HAM-based packages

1. INTRODUCTION

Nanolayers represent a paradigm shift in material science, offering a platform for groundbreaking innovations across various disciplines. Nanolayers, known for their structure consist of meticulously arranged materials, at the atomic level and measure just a few nanometers in thickness. This unique size gives nanolayers characteristics that set them apart from materials opening up a wide range of possibilities in different aspects such as energy storage, electronics, environmental and biomedicine cleanup. The key feature of nanolayers lies in their capability to manipulate substances on a scale level where quantum effects and surface interactions play a role. This ability allows for management of material properties, like conductivity, optical performance, mechanical durability and chemical reactivity. As a result, scientists and engineers are utilizing nanolayers to create materials, with functions exceeding the constraints of larger scale counterparts. The influence of nanolayers on the behavior of trihybrid NFs is studied by [1-3]. They also analyzed how microorganisms and variations in nanoparticle shapes affect this behavior in a two-disk setup. [4] conducted a study on fractional trihybrid nanoblood streaming in a diverging ciliated micro-vessel under strong electromagnetism. This study also incorporates a revised Hamilton-Crosser model to examine. Through a detailed analysis, [5] investigated the irreversibility and thermal characteristics of Cattaneo-Christov heat flux-based unsteady HNF. The flow was assumed over a rotating sphere, incorporating a mechanism of interfacial nanolayer. The hydrothermal oscillations of a radiative NF flow are examined by [6], with consideration for the diameter and nanolayer of the nanoparticles. An analogous study exploring nanolayers is mentioned in the references [7-11].

THNF are a type of engineered fluids that bring together the advantages of three elements; base fluids, nanoparticles, and additives. These crafted nanofluids, at the nanoscale aim to improve their heat conduction, light absorption, and flow characteristics showing potential for various uses, in heat transfer

and cooling systems. Essentially THNFs boast a blend of properties from their building blocks. The base fluid serves as the carrier medium, providing the primary heat transfer mechanism. Nanoparticles, typically metallic or oxide-based, are dispersed within a base fluid, enhancing thermal conductivity and heat transfer efficiency. Additives like surfactants or polymers stabilize the nanoparticle dispersion, resulting in THNFs with enhanced heat transfer coefficients, stability, and tunable rheological behavior. These NFs are used in automotive engines, solar thermal systems, and electronic cooling. [12] conducted a computational study on the entropy generation of Carreau THNF, enhancing the understanding of magnetohydrodynamics and entropy formation in ternary hybrid nanofluid systems. Oke's study explores heat and mass transfer in the three-dimensional magnetohydrodynamic flow of an ethylene glycol-based ternary hybrid nanofluid across a rotating surface [13]. [14] present a nonlinear analysis of Darcy-Forchheimer flow in an EMHD THNF (Cu-CNT-Ti/water) with a radiation impact. Saranya et al. [15] studied quartic autocatalysis on horizontal surfaces with asymmetric concentrations utilizing a water-based THNF including alumina, copper, and titania NPs. The list of resources [16-21] includes a comparable work studying ternary hybrid nanofluids.

The elements of blood encompassing cells, proteins, and various biomolecules serve as the fundamental components of blood-based NFs. Through the incorporation of NPs with specific functionality such as drug delivery vehicles or imaging agents, blood-based NFs utilize the inherent biocompatibility and transport properties of blood to achieve targeted delivery and improve diagnostic capabilities. A notable advantage of blood-based NFs is their capacity to transfer physiological barriers and engage with biological systems on a molecular level. This capability facilitates precise targeting of disease tissues, reducing off-target effects and enhancing therapeutic effectiveness. Due to these advantages, blood-based NFs are promising contenders for personalized medicine and targeted therapy. In diagnostic methodologies, they can be used for imaging and sensing by integrating contrast agents or biosensors in the bloodstream. This allows real-time monitoring of physiological coefficients. Early detection of disease assessment of therapeutic response are the benefits of this technology.

[22] presented a research on the potential of blood-based NFs as drug delivery vehicles through a perforated capillary. [23] revealed the blood-based flow of HNFs in the presence of a couple stresses and electromagnetic field. The study provides insights into the combined influence of these elements on fluid flow characteristics. Furthermore, serves as a foundation for optimizing system performance in various applications. [24] find out the influence of silver and gold NPs on fluid dynamics and heat transfer processes in blood-based nanofluids under pulsatile flow conditions. Al-Hussain and Tassaddiq's study on blood-based Casson HNFs explores the impact of viscosity variation on flow behavior and heat transfer mechanisms [25]. Similarly, researchers like [26-30] investigated on nanofluids flow of blood-based in a rotating channel, by introducing Casson model to study the flow dynamics, when the flow is subject to peristaltic motion, also with Cattaneo–Christov entropy generation and heat flux. The application of HNFs exhibits more effective transfer of heat than mono NFs due to the presence of dual metallic NPs within the base fluid [31-34].

Motivated by the above studies, this paper presents a mathematical model analyzing the effects of interfacial nanolayers on mass and heat transport in THNF flow. Investigating TiO_2, SiO_2, and Al_2O_3 in non-Newtonian biological fluids like blood, the research utilizes porous surfaces. Employing uniform transverse magnetic flux, the study transforms nonlinear PDEs into ODEs via similarity transformations, solved numerically and analytically. The findings of the research on the influence of interfacial nanolayers on mass and heat transport processes in THNF flow have various potential applications in different fields.

A significant area of application lies within biomedical engineering. Particularly in advancing drug delivery systems. It becomes possible to create more effective and precise drug carriers, by grasping how NF dynamics are influenced by interfacial nanolayers and the dispersion of NPs in non-Newtonian biological fluids such as blood. These carriers can be customized to navigate the intricate micro-environments within the body. Thus, enabling them to deliver therapeutic agents to specific tissues or cells with heightened precision and efficacy. Furthermore, optimizing mass and heat transfer phenomena is critical for enhancing energy efficiency and overall performance such as heat exchangers and cooling devices. Thus, the knowledge gained from this research can guide the development of innovative thermal management systems. Additionally, the study's numerical [35-37] and analytical [38-41] techniques for solving nonlinear equations and analyzing active parameters could be applied in various engineering disciplines beyond biomedical and thermal sciences, such as aerospace, automotive, and environmental engineering, where understanding flow of fluid and transport phenomena of heat is essential for designing and optimizing complex systems.

The magnetohydrodynamics flow of a nanofluid across an exponentially curved stretching surface was studied in detail by [42]. The governing equations are defined by applying the assumption to the curved stretching surface. An analytical approach is used to handle the governing system of equations. The results demonstrate that when the values of the magnetic parameter and porosity parameter grow, the velocity profile decreases. As the values of thermophoretic parameters and Brownian motion parameters rise, the temperature profile also rises. With a larger activation energy, the concentration profile is more robust.

The Darcy-Forchheimer flow caused by the curved stretch surface looped in a circle of radius R was studied by [43] in terms of heat and mass transfer. Chemical processes impact the flow via heat production and thermal radiation. The combination contains three kinds of nanoparticles: GO, ZrO_2, and SiO_2, with kerosene oil (KO) serving as the base fluid. This model incorporates convective heat conditions. The results show that GO is more influential on ZrO_2 and SiO_2. As the radiative flux and Biot number increase, the thermal distribution improves, but as the curvature factor increases, it worsens.

Through the gap of disk-cone devices, [44] investigated the flow of a Jeffrey fluid with dual diffusions, taking into account both non-Fick's and non-Fourier's assumptions. For fluid flow and heat transformation, four possible situations have been studied: 1. disc and cone are spinning in opposite directions; 2. disc and cone are spinning in the same direction; 3. cone is spinning but disc is stationary and 4. disc is spinning but cone is stationary. The transverse velocity panels always show retardation when the magnetic and Maxwell factors are large enough, regardless of whether the disc and cone are moving in the same direction, in opposing directions, or whether there is a static disc and a gyrating cone or a static cone and a gyrating disc.

In a ciliated stenotic/dilatant artery, blood flow patterns and heat transfer were investigated by [45]. The electro-magnetic effects on

blood infused with modified trihybrid nanoparticles (gold, copper, titania, and SWCNTs) with an interfacial nanolayer aspect are the main focus of this study. Due to its non-Newtonian nature, blood is represented using the fractional second grade fluid model. In a rapidly converging series, the homotopy perturbing method is used to solve the consequently highly nonlinear coupling flow equations. A decrease in blood flow due to fractional parameter and an increase in relaxation time in the central section of the ciliary stenosed arterial tract are both shown by the data.

Considering the combined effects of a heat source, buoyancy, viscoelastic, electro-osmotic, and Lorentz forces, [46] reported the outcomes of a mathematical simulation that assessed the haemodynamic effects of ternary hybrid nanoparticles infused into bloodstream via a diverging/converging ciliary micro-vessel. To solve the leading equations that were rescaled, the homotopic perturbing method was used. Compared to binary (89%) and unitary (48.3%) nanoparticles, ternary nanoparticles have superior physio-thermal characteristics when injected into the circulation (117.6%).

In their groundbreaking model, [47] was able to replicate the behaviour of tetra-hybrid nanoparticles covered with nanolayers as they moved through an electrified permeable diseased artery carrying Jeffrey's blood while subjected to an electromagnetic field. Titania (TiO_2), Cu (Cu), Au (Au) nanoparticles, and single-walled carbon nanotubes (SWCNTs) are all added to blood, the base fluid, to create tetra-hybrid nanoblood. A smaller fractional parameter, which represents short memory effects, results in quicker blood flow compared to the integer-order model, according to key findings. Electroosmotic forces, Lorentz forces, and stenotic height all have a large impact on blood velocity and raise the velocity profile dramatically.

To address the issue of wall slide in two-dimensional blood flow via an angled catheterised artery with numerous stenoses, [48] presented a theoretical analysis of ternary hybrid nanoparticles (Cu-Ag-Au). Graphs showing the flow properties of tri-hybrid (Cu-Ag-Au), hybrid (Cu-Au), and single-audit (Au) nanofluids through arteries with composite stenosis are shown in the research. To speed up the heat transfer process, the model incorporates tri-hybrid nanoparticles and uses thermal radiation. Findings reveal that flow velocity and magnetic field growth are strongly regulated by magnetic force, in contrast to the inverse effect caused by a rise in the radiation parameter. Thermal slip improves the distribution of temperatures, whereas magnetic force and radiative heat decrease the pressure gradient and temperature in blood flow, respectively.

[49] studied the flow of a hybrid nanofluid containing Au and Fe_3O_4 through a stenotic artery that is constricted. An angled magnetic field and temperature-dependent thermal conductivity are included in a mathematical analysis of the Au-Fe_3O_4/blood flow behaviour in the stenosis zone. To compare the findings of flow characteristics and heat transmission, the tube catheter model and the balloon catheter model are examined separately. The qualities of the walls at the channel borders are thermal slip and second-order velocity slip. The findings show that the magnetic force causes the velocity profile to grow, whereas the thermal conductivity of the nanofluid causes the opposite tendency. In order to regulate and prevent cardiovascular illnesses, interfacial nanolayers of nanoparticles considerably change blood temperature.

This research unveils its uniqueness through the thorough analytical and numerical evaluation of nanolayer effects on mass transfer in THNFs with blood and other non-Newtonian fluids when subjected to uniform transverse magnetic flux and porous surfaces. This study brings together TiO_2-SiO_2 and Al_2O_3 nanoparticles through the combination of ADM and ERKM to solve its converted nonlinear mathematical equations. The analysis provides original findings about the co-existential interaction of unsteadiness together with magnetic fields in combination with nanoparticle volume fractions that influence flow dynamics as well as thermal behavior and material concentration distributions while introducing new information applicable to biomedical engineering domains and drug delivery frameworks and thermal management systems. The obtained results from this work enhances knowledge about THNF behaviors under complex conditions while filling existing gaps in existing research.

2. GOVERNING EQUATIONS

Let us consider the blood to be a non-Newtonian biological base fluid on 2D MHD laminar incompressible THNF flow through a permeable channel of width $2a(t)$ with both effects (i.e. chemical reaction and dissipation of viscous). The mixture between the base fluid and the three NP is in thermal equilibrium. Both the walls of channel have the same permeability and are capable of moving with the time-dependent rate $a'(t)$. The flow configuration of this problem is displayed in Figure 1.

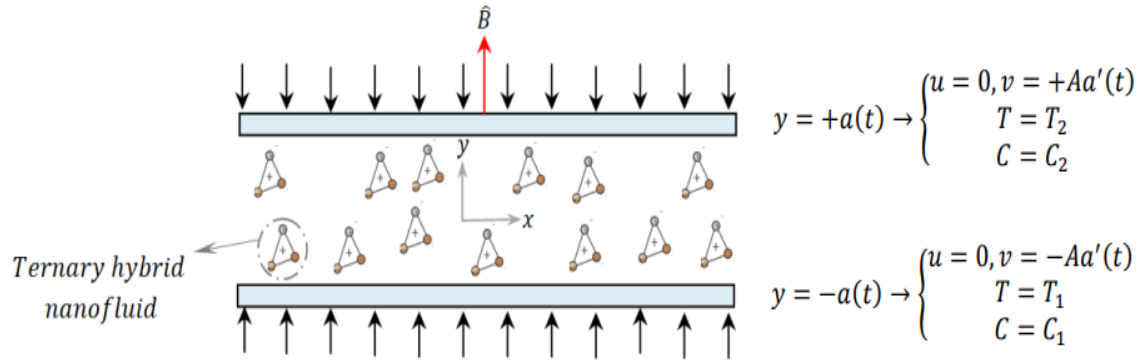

Fig. 1. Physical model

The Navier-Stokes equations are [50,51].

$$\frac{\partial u}{\partial x}+\frac{\partial v}{\partial y}=0, \tag{1}$$

$$\rho_{thnf}\left(\frac{\partial u}{\partial t}+u\frac{\partial u}{\partial x}+v\frac{\partial u}{\partial y}\right)=-\frac{\partial P}{\partial x}+\mu_{thnf}\nabla^2 u-\sigma_{thnf}B_0^2 u \tag{2}$$

$$\rho_{thnf}\left(\frac{\partial v}{\partial t}+u\frac{\partial v}{\partial x}+v\frac{\partial v}{\partial y}\right)=-\frac{\partial P}{\partial y}+\mu_{thnf}\nabla^2 v \tag{3}$$

$$\frac{\partial T}{\partial t}+u\frac{\partial T}{\partial x}+v\frac{\partial T}{\partial y}=\frac{k_{thnf}}{(\rho c_p)_{thnf}}\nabla^2 T+\frac{\mu_{thnf}}{(\rho c_p)_{thnf}}\left(\frac{\partial u}{\partial y}\right)^2 \tag{4}$$

$$\frac{\partial C}{\partial t}+u\frac{\partial C}{\partial x}+v\frac{\partial C}{\partial y}=D\nabla^2 C-K_0(C-C_2) \tag{5}$$

Here σ_{thnf}, μ_{thnf}, ρ_{thnf} , υ_{thnf}, $(\rho Cp)_{thnf}$, k_{thnf} , D_B and D_T stand for the electrical conductivity, the viscosity of ternary hybrid nanofluid, the density of THNF, the kinematic viscosity of THNF, the specific heat capacitance of THNF, the thermal conductivity of THNF, the Brownian coefficient of diffusion and the coefficient of thermophoresis diffusion, respectively.

With boundary conditions introduced as [50,51].

$$\text{At } y=-a(t)\rightarrow u=0, v=-Aa'(t), T=T_1 \text{ and } C=C_1 \tag{6}$$

$$\text{As } y=+a(t)\rightarrow u=0, v=+Aa'(t), T=T_2 \text{ and } C=C_2 \tag{7}$$

The boundary conditions specified in Eqs. (6) and (7) represent the physical constraints of the flow system at the channel walls. At y=−a(t), the no-slip condition (u=0) ensures the fluid velocity is zero relative to the wall, while the vertical velocity (v=−Aa'(t)) accounts for suction or injection effects due to wall permeability. The fixed temperature ($T=T_1$) and concentration ($C=C_1$) conditions model the thermal and mass transfer properties at the lower wall. Similarly, at y=+a(t), the conditions mirror these effects for the upper wall, with v=+Aa'(t) indicating the opposite direction of fluid injection or suction. These conditions are essential for capturing the realistic behavior of the ternary hybrid nanofluid in a porous channel, including the interplay of fluid dynamics, heat transfer, and mass diffusion, which are critical for applications like drug delivery and thermal management systems.

The properties of THNF and the thermo-physical characteristics of conventional liquid (Blood) and NPS are presented in Tables 1 and 2, respectively.

Tab. 1. A characteristic made between the physical features of ternary hybrid nanofluids.

Dynamic viscosity	$\mu_{thnf}=\frac{\mu_f}{(1-\varphi_{\mathrm{TiO_2}})^{2.5}(1-\varphi_{SiO_2})^{2.5}(1-\varphi_{\mathrm{Al_2O_3}})^{2.5}}$
Density	$\rho_{thnf}=(1-\varphi_{\mathrm{TiO_2}})\left((1-\varphi_{SiO_2})\left((1-\varphi_{\mathrm{Al_2O_3}})\rho_f+\varphi_{\mathrm{Al_2O_3}}\rho_{\mathrm{Al_2O_3}}\right)+\varphi_{SiO_2}.\rho_{SiO_2}\right)+\varphi_{\mathrm{TiO_2}}.\rho_{\mathrm{TiO_2}}$
Specific heat	$(\rho C_p)_{thnf}=(1-\varphi_{\mathrm{TiO_2}})\left((1-\varphi_{SiO_2})\left((1-\varphi_{\mathrm{Al_2O_3}})(\rho C_p)_f+\varphi_{\mathrm{Al_2O_3}}(\rho C_p)_{\mathrm{Al_2O_3}}\right)+\varphi_{SiO_2}.(\rho C_p)_{SiO_2}\right)+\varphi_{TiO_2}.(\rho C_p)_{TiO_2}$
Electrical Conductivity	$\begin{cases}\frac{\sigma_{thnf}}{\sigma_{hnf}}=1+\frac{3\left(\frac{\sigma_{TiO_2}}{\sigma_{hnf}}-1\right)\varphi_{TiO_2}}{\left(\frac{\sigma_{TiO_2}}{\sigma_{hnf}}+2\right)-\varphi_{TiO_2}\left(\frac{\sigma_{TiO_2}}{\sigma_{hnf}}-1\right)}\\ \frac{\sigma_{hnf}}{\sigma_{nf}}=1+\frac{3\left(\frac{\sigma_{SiO_2}}{\sigma_{nf}}-1\right)\varphi_{SiO_2}}{\left(\frac{\sigma_{SiO_2}}{\sigma_{nf}}+2\right)-\varphi_{SiO_2}\left(\frac{\sigma_{SiO_2}}{\sigma_{nf}}-1\right)}\\ \frac{\sigma_{nf}}{\sigma_f}=1+\frac{3(\frac{\sigma_{\mathrm{Al_2O_3}}}{\sigma_f}-1)\varphi_{\mathrm{Al_2O_3}}}{\left(\frac{\sigma_{\mathrm{Al_2O_3}}}{\sigma_f}+2\right)-\varphi_{\mathrm{Al_2O_3}}\left(\frac{\sigma_{\mathrm{Al_2O_3}}}{\sigma_f}-1\right)}\end{cases}$
Thermal Conductivity	$\begin{cases}\frac{k_{thnf}}{k_{hnf}}=\frac{k_{TiO_2}+2k_{hnf}-2\varphi_{TiO_2}(k_{hnf}-k_{TiO_2})}{k_{TiO_2}+2k_{hnf}-\varphi_{TiO_2}(k_{hnf}-k_{TiO_2})}\\ \frac{k_{hnf}}{k_{nf}}=\frac{k_{SiO_2}+2k_{nf}-2\varphi_{SiO_2}(k_{nf}-k_{SiO_2})}{k_{SiO_2}+2k_{nf}-\varphi_{SiO_2}(k_{nf}-k_{SiO_2})}\\ \frac{k_{nf}}{k_f}=\frac{k_{\mathrm{Al_2O_3}}+2k_f-2\varphi_{\mathrm{Al_2O_3}}(k_f-k_{\mathrm{Al_2O_3}})}{k_{\mathrm{Al_2O_3}}+2k_f-\varphi_{\mathrm{Al_2O_3}}(k_f-k_{\mathrm{Al_2O_3}})}\end{cases}$

Tab. 2. Thermophysical characteristics of a ternary hybrid nanofluid

Physical properties	$\rho\ (kg/m^3)$	$C_p(J/kg.°K)$	$k(W/m.°K)$	$\sigma(S/m)$
Blood	1063.8	3594	0.492	0.8
$TiO_2 \rightarrow \varphi_1$	4250	397.2	8.9538	2.4×10+6
$SiO_2 \rightarrow \varphi_2$	2200	765	1.4013	3.5×10+6
$Al_2O_3 \rightarrow \varphi_3$	3970	686	40	36.9×10+6

Considering the following transformations [51].

$$\begin{cases} \eta = \frac{y}{a} \\ u = \frac{-xv_f}{a^2} f'(\eta) \\ v = \frac{v_f}{a} f(\eta) \\ \theta = \frac{T-T_2}{T_1-T_2} \\ \varphi = \frac{C-C_2}{C_1-C_2} \end{cases} \quad (8)$$

The use of the similarity transformation, which is represented by equation (8), provides us with the coupling equations for the velocity, temperature and mass concentration profiles as:

$$\frac{A_1}{A_2} f'''' + \alpha(3f'' + \eta f''') + Re(f'f'' - ff''') - A_2{}^{-1} A_3 M f'' = 0 \quad (9)$$

$$A_4\theta'' + A_5 Pr\theta'(\eta\alpha - fRe) + A_1 Br\, Re^2 f''^2 = 0 \quad (10)$$

$$\varphi'' + Sc\, \varphi'(\eta\alpha - f\, Re) - K_r\varphi = 0 \quad (11)$$

With boundary conditions:

$$At\ \eta = -1 \rightarrow f = -1, f' = 0,\ \theta = 1\ and\ \ \varphi = 1 \quad (12.1)$$

$$As\ \eta = +1 \rightarrow f = +1, f' = 0,\ \theta = 0\ and\ \ \varphi = 0 \quad (12.2)$$

The parametric values are defined in Table 3. Also, From Eq. (9-11), the quantities A_1, A_2, A_3, A_4 and A_5 are as follows in Table 4.

Tab. 3. Explanation of the parameter control constraints

Symbol	Name	Formula
α	Time-dependent dimensionless parameter	$\frac{a(t)a'(t)}{v_f}$
Re	Reynolds number	$\frac{A\alpha a'}{v_f}$
Sc	Schmidt numbers	$\frac{v_f}{D_B}$
Ec	Eckert number	$\frac{v^2}{\Delta T(C_P)_{bf}}$
M	Hartmann number	$\sqrt{\frac{\sigma_f a^2 B_0^2}{\mu_f}}$
Pr	Prandtl number	$\frac{\rho_f . C_{Pf} . f_{max}}{k_f}$
Br	Brinkman number	$Pr * Ec$

Tab. 4. Explanation of the quantities control constraints

Symbol	Formula
A_1	$(1-\varphi_{TiO_2})^{-2.5}(1-\varphi_{SiO_2})^{-2.5}(1-\varphi_{Al_2O_3})^{-2.5}$
A_2	$(1-\varphi_{TiO_2})\left((1-\varphi_{SiO_2})\left((1-\varphi_{Al_2O_3}) + \varphi_{Al_2O_3}\frac{\rho_{Al_2O_3}}{\rho_f}\right) + \varphi_{MoS_2}.\frac{\rho_{MoS_2}}{\rho_f}\right) + \varphi_{TiO_2}.\frac{\rho_{TiO_2}}{\rho_f}$
A_3	$\frac{\sigma_{thnf}}{\sigma_f}$
A_4	$\frac{k_{thnf}}{k_f}$
A_5	$(1-\varphi_{TiO_2})\left\{(1-\varphi_{SiO_2})\left[(1-\varphi_{Al_2O_3}) + \varphi_{Al_2O_3}\frac{(\rho C_p)_{Al_2O_3}}{(\rho C_p)_f}\right] + \varphi_{SiO_2}.\frac{(\rho C_p)_{SiO_2}}{(\rho C_p)_f}\right\} + \varphi_{TiO_2}.\frac{(\rho C_p)_{TiO_2}}{(\rho C_p)_f}$

The key assumptions of our mathematical model:

1. Under this model the fluid motion stays laminar while being incompressible since turbulence effects receive no consideration.
2. The particles and base fluid exist in thermodynamic equilibrium so that no localized temperature gradients occur.
3. The model incorporates a homogenous transverse magnetic field that generates no meaningful effects on the induced electric field.
4. Treatment of the ternary hybrid nanofluid as a single-phase medium represents it as a homogeneous structure without considering particle agglomeration.
5. The model does not include thermal radiation or viscous dissipation unless specific modeling occurs.
6. Researchers make the assumption that spherical nanoparticles
7. maintain uniform dimensions throughout distribution while maintaining consistent size.
8. For easier calculations velocity slip and temperature jump effects at boundaries are omitted.

3. APPLICATION OF ADM METHOD

This portion of the work illustrates the procedure of the scheme. Here, the set of ODEs (9) to (11) along with boundary conditions (12) are solved computationally via ADM and Explicit Runge-Kutta Method (ERKM) approaches. Moreover, the flow chart has been shown in Figure 2, so that, the readers can easily understand the background of the method.

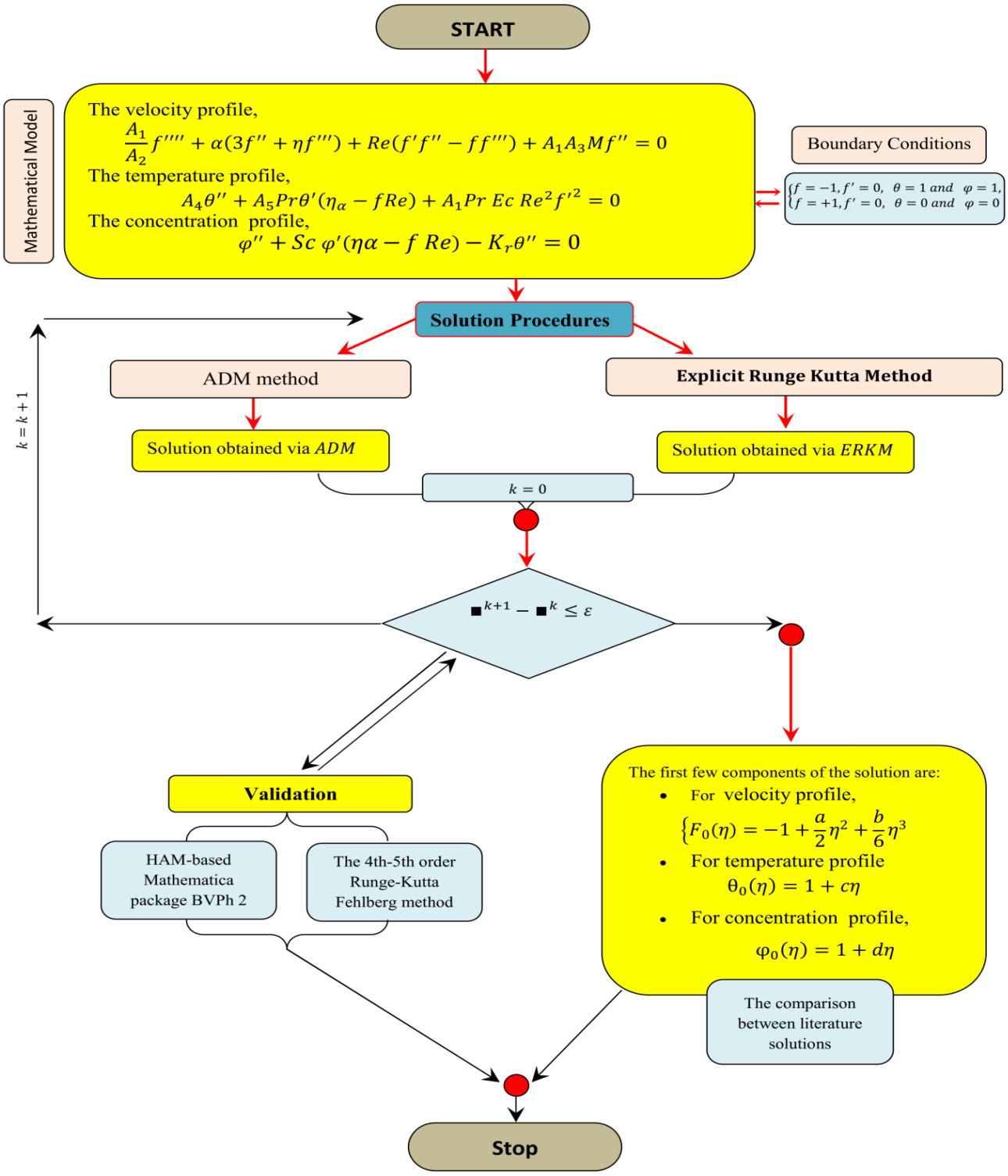

Fig. 2. ADM procedure

4. DISCUSSION OF RESULTS

In this section, we present the outcomes and interpretations of our investigation into the influence of interfacial nanolayers on mass and heat transfer phenomena within THNF flow, particularly focusing on non-Newtonian biological fluids such as blood. Through comprehensive numerical simulations and graphical representations, we delve into the impact of active parameters on various aspects of the system, examining their influence on heat and mass transfer processes. We contextualize our findings within the broader framework of existing knowledge, highlighting both the confirmations and deviations from previous studies. Moreover, we discuss the implications of our results, exploring potential avenues for future research and shedding light on the underlying mechanisms governing THNF flow in non-Newtonian biological fluids. For visualized Figures 3,4,5,6 and 8, it is worth to mention the existence of cross-over-point, at the middle of channel, which worthy shows the reverse behaviour in the evolution of temperature and concentration profiles between lower and upper regions of the channel. However, for the velocity distribution, we clearly notice the existence of two cross-over-points near the channel centerline.

The interaction between unsteadiness and velocity, concentration, and temperature profiles are shown in Figure 3. For the range of -0.5 to 0.5 values of the similarity parameter, where the effects of porous surfaces are less pronounced, the influence of unsteadiness may lead to increased velocity profiles near the channel centerline. In fact, unsteadiness enhances mixing and convective flow, resulting in higher velocity profiles. With negative values of the similarity parameter ranging from -0.5 to -1, increasing unsteadiness can interrupt flow and diminish velocity profiles due to higher flow fluctuations. In this circumstance, the momentum boundary layer thickness boosts and consequently the reversal flow apparition is highly favoured. In contrast, with positive similarity parameter ranging from 0.5 to 1, where blowing effects are dominant, increasing unsteadiness also makes decrease the fluid velocity that leads to momentum boundary layer thickness increase and hence the backflow phenomenon can start. Unsteadiness with negative similarity factors can improve fluid mixing and convective heat transfer, thus raising the temperature and concentration profiles. However, with positive similarity parameters (0 to 1), when blowing effects are dominant, increased unsteadiness can disrupt flow patterns and impede convective heat transfer, resulting in flow instabilities and lower temperature and concentration profiles.

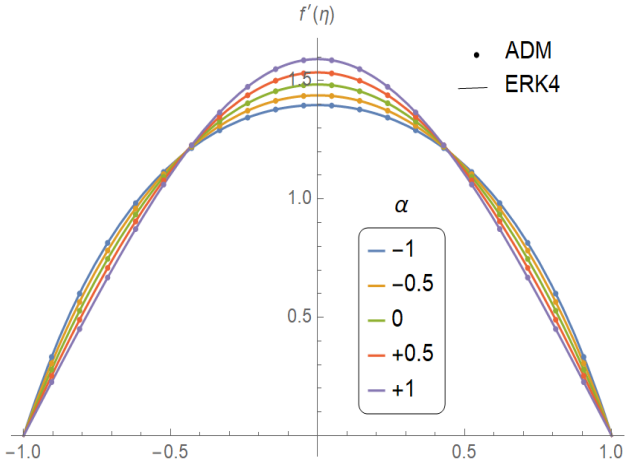

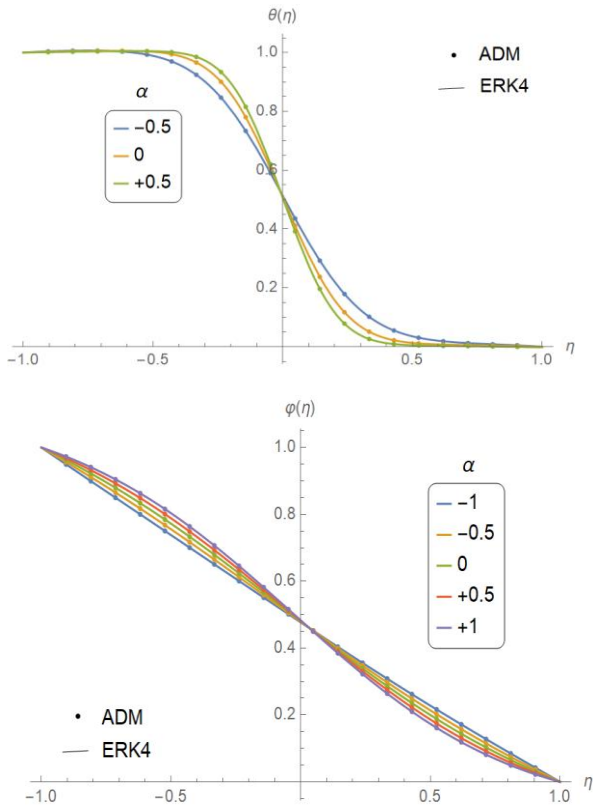

Fig. 3. Influence of α on f', θ and φ when: $\varphi_1 = \varphi_2 = \varphi_3 = 0.01, Re = -1,\ M = 1, Sc = 1, Kr = 0.1$ and $Pr = 21$

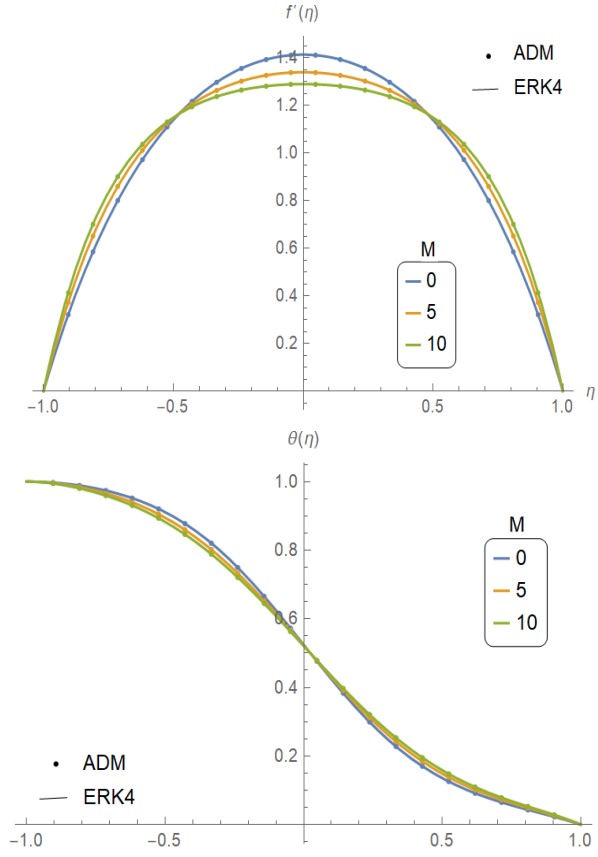

Fig. 4. Influence of M on f' and θ when: $\varphi_1 = \varphi_2 = \varphi_3 = 0.01, Re = -1,, \alpha = -1, Sc = 1, Kr = 0.1$ and $Pr = 21$

Figures 4 demonstrate the effect of magnetic parameter M on velocity and temperature profiles. As previously stated, for negative similarity parameters (-1 to -0.5), when suction effects are dominant, raising the magnetic parameter may improve fluid mixing and convective flow. In suction-dominated locations, a greater magnetic field can generate fluid motion and boost velocity profiles where the momentum boundary layer thickness drops and consequently the reversal flow is entirely vanished. On the other hand, for positive similarity parameters varying from 0.5 to 1, when blowing effects are dominant, raising the magnetic component may also enhance flow patterns and convective flow. The stronger magnetic field generate the well-known Lorentz force that opposes to the flow direction and eliminates any defect in the flow structure. As a consequence, the thickness of momentum boundary layer decrease leading to the backflow vanishment.

Similarly, in Figure 4 for negative similarity parameters varying from -1 to 0, where suction effects are prevailing, raising the magnetic parameter may reduce convective heat transmission. In places where suction effects dominate, a larger magnetic field can lower temperature profiles. On the other hand, for positive similarity parameters varying from +1 to 0, when blowing effects are predominant, raising the magnetic parameter may improve convective heat transfer. In areas where blowing effects predominate, a greater magnetic field can generate fluid motion and raise temperature profiles.

Figure 5 illustrates the impact of Reynolds number on the velocity profile of a ternary hybrid nanofluid through porous surfaces. The Reynolds number, a dimensionless parameter, determines the ratio of inertial and viscous forces in fluid flow. The similarity parameter (η) is varied between -1 and 1, with the Reynolds number varying from -1 to 1 causing the flow to be laminar or creeping. Consequently, the influence of Reynolds number on the velocity profile is minimal within this range. The velocity profile tends to exhibit a smooth, parabolic distribution, typical of laminar flow through porous media. Thus, the influence of Reynolds number on the velocity profile of a ternary hybrid nanofluid through porous surfaces decreases at the level of channel centerline within the laminar regime ($\eta \in [-0.5, +0.5]$) where viscous forces dominate, while it increases near the channel walls at the level of upper half of the channel ($\eta \in [0.5, 1]$) and lower half of the channel ($\eta \in [-0.5, -1]$) due to the growing significance of inertial forces. At these zones, the thickness of momentum boundary layer drops and consequently the reversal flow is entirely disappeared.

Figure 6 depicts the concentration and temperature distribution plotted against the influence of Reynolds number and similarity parameter for a THNF between two porous surfaces. The similarity parameter characterizes the influence of porous surfaces on the flow and transfer of heat. As the similarity parameter varies, the impact of the porous surfaces on the flow and heat transfer changes. A negative similarity parameter typically represents suction effects, where fluid is drawn into the porous surfaces, affecting the velocity, concentration, and temperature distribution. A positive similarity parameter represents blowing effects, where fluid is expelled from the porous surfaces, altering the flow, temperature, and concentration distributions. Consequently, higher Reynolds numbers tend to enhance rates of heat transport due to enhanced convective transfer of heat. From Figure 6, the reduce in the concentration and temperature profiles between -1 to 0 values of the similarity parameter is attributed to stabilizing suction effects, which maintain a more uniform temperature and concentration distribution. Conversely, the increase in the temperature and concentration profiles from 0 to 1 values of the similarity parameter is influenced by disruptive blowing effects, which lead to non-uniform temperature and concentration distributions. These effects interact with changes in Reynolds number, which can either enhance or diminish the influence of convective transfer of heat on the distribution of temperature.

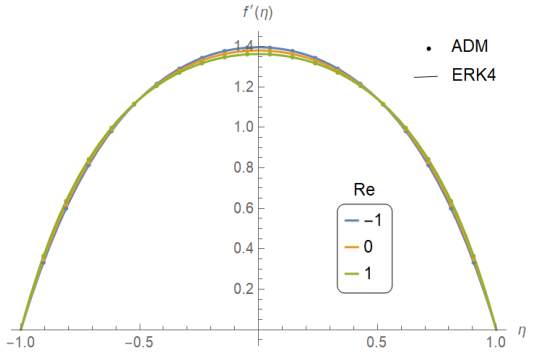

Fig. 5. Influence of Re on f' when: $\varphi_1 = \varphi_2 = \varphi_3 = 0.01, \alpha = -1, Sc = 1, Kr = 0.1$ and $Pr = 21$

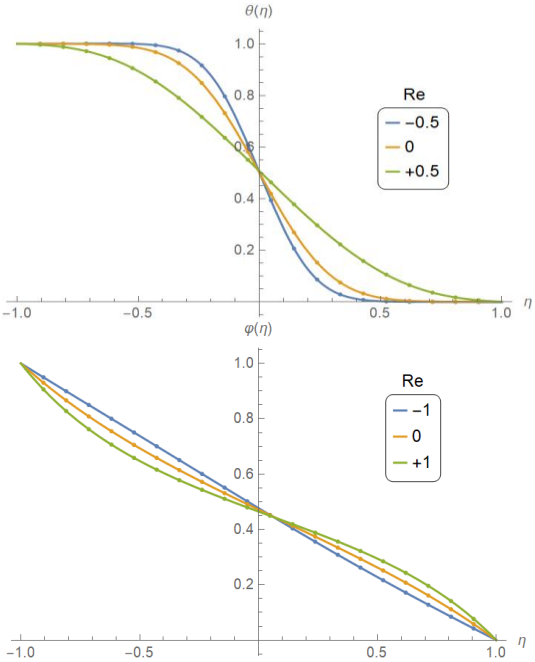

Fig. 6. Influence of Re on $\theta(\eta)$ and $\varphi(\eta)$ when: $\varphi_1 = \varphi_2 = \varphi_3 = 0.01,\ \alpha = -1, Sc = 1, Kr = 0.1$ and $Pr = 21$

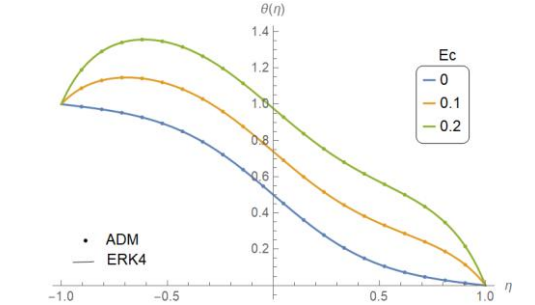

Fig. 7. Influence of Ec on θ when: $\varphi_1 = \varphi_2 = \varphi_3 = 0.01,\ Re = -1, \alpha = -1, Sc = 1$ and $Kr = 0.1$

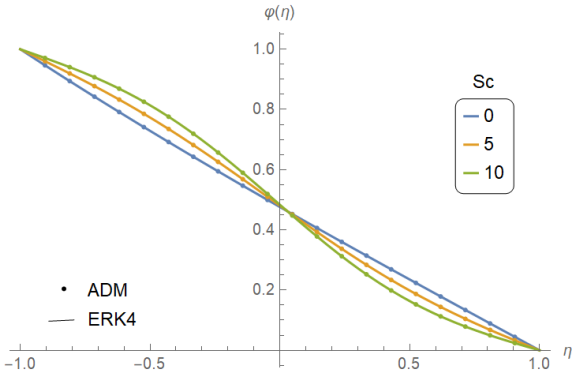

Fig. 8. Influence of Sc on θ when: $\varphi_1 = \varphi_2 = \varphi_3 = 0.01,\ Re = -1, \alpha = -1, M = 1, Kr = 0.1 \ \ and\ Pr = 21$

Figure 7 presents a visual depiction of how temperature changing within the system as the Eckert number is varied. As the value of the Eckert number is increased, the temperature profile tends to increase due to more efficient thermal boundary layer behavior within the flow field. In flows with higher Eckert numbers, the thermal boundary layer tends to be thinner and more dynamic due to enhanced mixing and convective heat transfer. This thinner boundary layer allows for more efficient transfer of heat between the fluid and the solid surfaces, leading to higher temperatures within the boundary layer and an overall increase in the temperature profile.

The behavior of the concentration distribution with changes in the Schmidt number and similarity parameter is explained in Figure 8. Higher Schmidt numbers enhance momentum diffusivity relative to mass diffusivity, leading to increased concentration profiles in the presence of suction effects (negative similarity parameters). Conversely, as the Schmidt number increases, mass diffusivity dominates, resulting in decreased concentration profiles in the presence of blowing effects (positive similarity parameters).

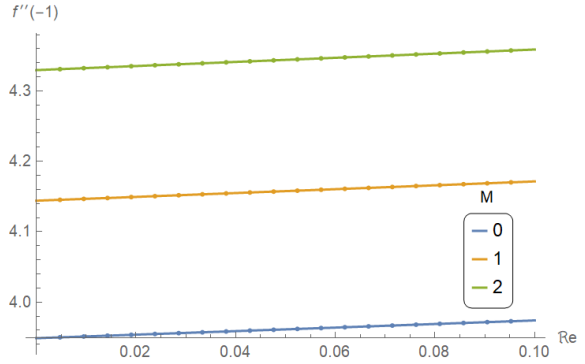

Fig. 9. Influence of both Re and M on f'' when: $\varphi_1 = \varphi_2 = \varphi_3 = 0.01,\ Re = -1, \alpha = -1, Kr = 0.1 \ \ and\ Pr = 21$

Figure 9 conducted a thorough examination to predict the impact of the magnetic parameter in association with Reynolds number on microorganism skin friction coefficient. Clearly, the friction coefficient increases as M and Re increases. The magnetic field influences the formation and behavior of the boundary layer along the porous surfaces. As the magnetic parameter increases, the magnetic forces alter the boundary layer dynamics, leading to increased interaction between the surfaces and fluid. This enhanced interaction results in higher skin friction along the surfaces. In this situation, the reversal flow is entirely disappeared due to the stabilizing impact of the MF.

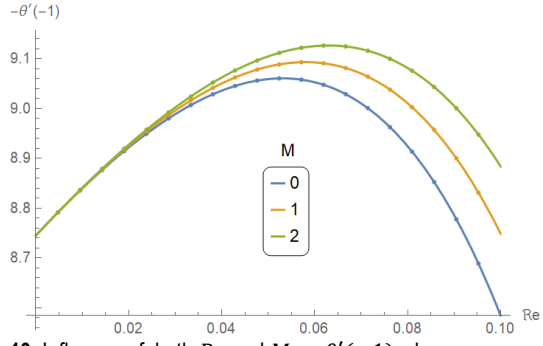

Fig. 10. Influence of both Re and M on $\theta'(-1)$ when: $\varphi_1 = \varphi_2 = \varphi_3 = 0.01,\ \alpha = -1, Kr = 0.1 \ \ and\ Pr = 21$

Figure 10 illustrates the relationship between the rate of heat transport and the magnetic parameter jointly with Reynolds number within the system. The MF may enhance transfer of heat by promoting better mixing and convective transfer of heat within the fluid. This can result in higher Nusselt numbers as the magnetic parameter enhances, especially in the laminar flow regime. The MF can also affect the boundary layer dynamics and induce more effective heat transfer from the solid surfaces to the fluid, further contributing to the increase in Nusselt number. Secondly, as Reynolds number increases, the behavior of NPs within the fluid and their interaction with the porous surfaces may change, affecting the overall heat transfer characteristics. Beyond a certain critical Reynolds number, the Nusselt number begins to drop. This is because the interaction between the porous surfaces and fluid flow becomes more complex, potentially altering the heat transfer characteristics in unexpected ways.

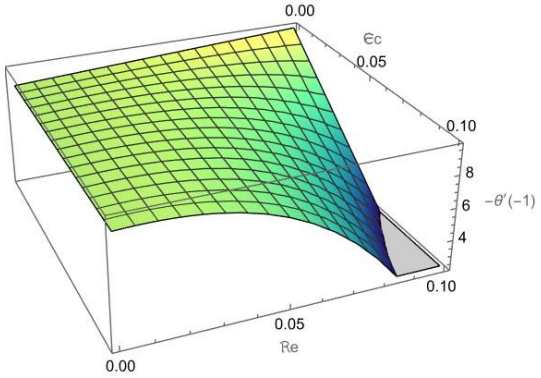

Fig. 11. Influence of both Re and Ec on $-\theta'(-1)$ when: $\varphi_1 = \varphi_2 = \varphi_3 = 0.01, \alpha = -1, Kr = 0.1\ M = 1 \ and\ Pr = 21$

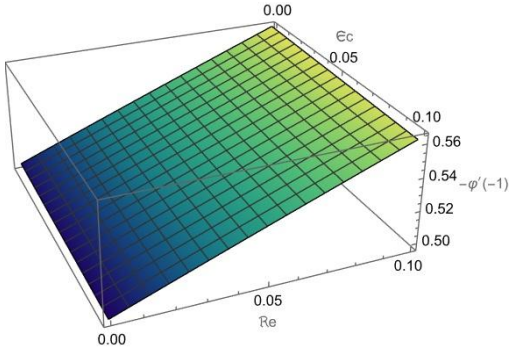

Fig. 12. Influence of both Re and Ec on $\varphi'(-1)$ when: $\varphi_1 = \varphi_2 = \varphi_3 = 0.01,\ \alpha = -1, Kr = 0.1\ M = 1 \ and\ Pr = 21$

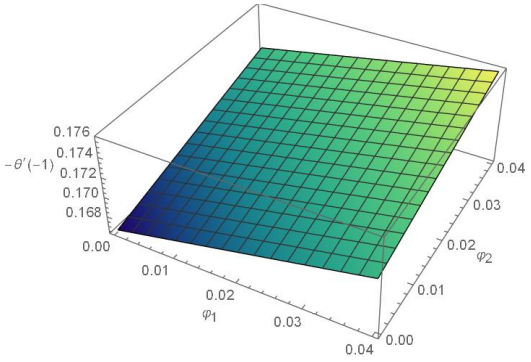

Fig. 13. Influence of both φ_1 and φ_2 on $\varphi'(-1)$ when: $Re = -1, Ec = 0.01, \varphi_3 = 0.01, \alpha = -1, Kr = 0.1\ M = 1\ and\ Pr = 21$

Figures 11-13 analyze the surface plot showing the performance of parameters like Eckert number and Reynolds number on the rate of heat transport; Schmidt number and parameter of chemical reaction on rate of mass transfer; and NP volume fractions on the rateof heat transport. From the Figure 11 is it visible that higher Reynolds and Eckert numbers typically lead to decreased heat transfer rate, as Reynolds number increases, the boundary layer thickness near the heat transfer surface may also increase. A thicker boundary layer can result in reduced convective heat transfer rates as the thermal gradient between the fluid and the surface decreases. While at elevated Eckert numbers, the behaviour of the thermal boundary layer near the heat transfer surface may change. The increased kinetic energy in the flow may alter the thickness and structure of the boundary layer, affecting convective heat transfer. This change in boundary layer behaviour may result in reduced heat transfer rates. In addition, it is highly stated that he optimal conditions leading to the better heat transfer rate (higher Nusselt number) are achieved with higher values of Reynold number and lower values of Eckert number.

Meanwhile Figure 12 shows decreased mass transfer rates with the Schmidt number. A higher Schmidt number may indicate a smaller mass diffusivity relative to momentum diffusivity, leading to a thicker concentration boundary layer. This thicker boundary layer can create a larger resistance to mass transfer, resulting in decreased mass transfer rates. Also, as the parameter of chemical reaction accelerates, the reaction rate enhances, leading to quick consumption of reactants. This can create a concentration gradient near the reactant interface, which, in turn, drives mass transfer. However, if the rate of reaction becomes too high, it may deplete the concentration gradient, reducing the driving force for mass transfer and ultimately decreasing the mass transfer rate. The lower mass transfer rate is thus gained with the combination of higher values of both Kr and Sc; however, the lower mass transfer rate is achieved with lowest values of Kr and Sc.

NPs typically have larger thermal conductivities compared to the base fluid. When NPs are dispersed in the fluid, they act as conductive pathways for heat transfer. As the volume fraction of NPs enhances, so does the overall NF thermal conductivity. This allows for more efficient heat conduction through the NF, leading to increased heat transport rates as shown in Figure 13 where the improved heat transfer rate is occurred at higher values of both nanoparticles volume fraction φ_1 and φ_2.

Tab. 5. Effects of φ on the $\mathrm{f}'(0)$ and $\theta(0)$ when $Re = \alpha = -1, Kr = M = Sc = 1\ and\ Pr = 21$

	$\boldsymbol{\varphi_{TiO_2}}$	$\boldsymbol{\varphi_{SiO_2}}$	$\boldsymbol{\varphi_{Al_2O_3}}$	$\boldsymbol{f''(-1)}$	$\boldsymbol{\theta'(-1)}$
N-F	0%	0%	0%	1.4067241	0.5258221
	2%	0%	0%	1.3993983	0.52438206
	0%	2%	0%	1.4016671	0.5247220
	0%	0%	2%	1.3987235	0.52430242
	φ_{TiO_2}	φ_{SiO_2}	$\varphi_{Al_2O_3}$	$f''(-1)$	$\theta'(-1)$
HN-F	0%	0%	0%	1.4067241	0.5258221
	2%	2%	0%	1.3941953	0.52334135
	0%	2%	2%	1.39345981	0.5232619
	2%	0%	2%	1.39123039	0.522949
	φ_{TiO_2}	φ_{SiO_2}	$\varphi_{Al_2O_3}$	$f''(-1)$	$\theta'(-1)$
THN-F	0%	0%	0%	1.4067241	0.5258221
	1%	1%	1%	1.3965176	0.52382605
	2%	2%	2%	1.3858312	0.52196548
	0%	0%	2%	1.3746924	0.52023433

*The table nanoparticles dispersed in the base fluid. These concentrations could vary from low to high values, representing different levels of nanoparticle loading in the nanofluid

5. COMPARISON AND VALIDATION

We compared our numerical solutions obtained applying the ADM and the Explicit Runge-Kutta Method to those found using the HAM-based Mathematica package. This comparative analysis allowed us to evaluate the consistency and accuracy of our computational methodologies. The convergence of results, as demonstrated in Figure 14, shows the reliability of both computational approaches for capturing the intricate dynamics of THNF flow in non-Newtonian biological fluids. The tabulated data in Table 6 offers quantitative insights into the agreement between the numerical solutions obtained through ADM and Explicit Runge-Kutta method. The alignment between numerical solutions derived from different methodologies validates the accuracy of our results. This agreement also enhances our confidence in the predictive capability of our mathematical model.

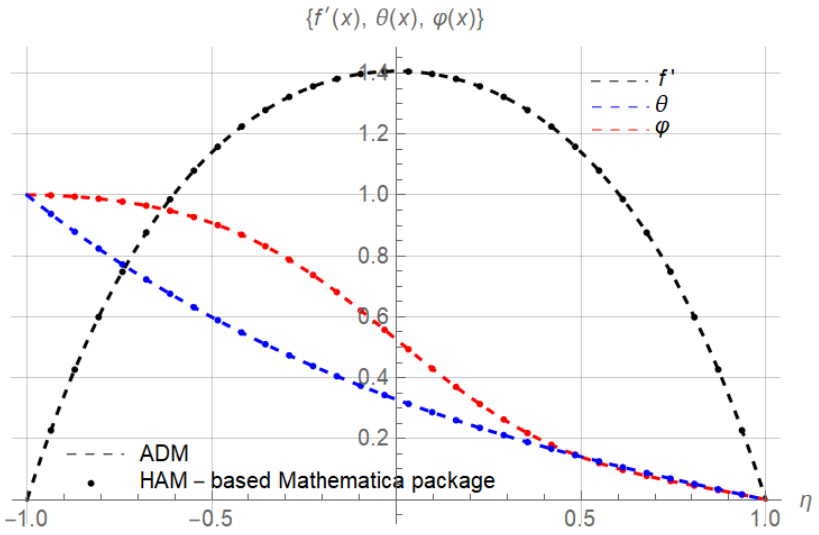

Fig. 14. Comparison of f', θ and φ with HAM-package when : $Re = \alpha = -1, Kr = M = Sc = 1$ *and* $Pr = 21$

Tab. 6. Comparison for $f''(-1)$, $\theta'(-1)$ and $\varphi\theta'(-1)$ when $\alpha = 1, \varphi = 0.06, \mathrm{Kr} = 0.1, \mathrm{Ec} = 0, \mathrm{M} = 1, \mathrm{Sc} = 1$ and $\mathrm{Pr} = 6.2$

Re	$f''(-1)^{[51]}$	$f''(-1)^{ADM}$	$\theta'(-1)^{[51]}$	$\theta'(-1)^{ADM}$	$\varphi'(-1)^{[51]}$	$\varphi'(-1)^{ADM}$
-1	2.00603	2.00603	−0.0041705	−0.0041705	−0.263183	−0.263182
0	1.83493	1.83492	−0.072609	−0.072607	−0.405111	−0.405111
$+1$	1.53430	1.53430	−0.730132	−0.730132	−0.610916	−0.610916

6. CONCLUSION

In this study, we look at how interfacial nanolayers affect mass and heat transport in THNF flow. Our attention is mostly on non-Newtonian biological fluids like blood. We include the presence of TiO_2, SiO_2, and Al_2O_3 on porous surfaces in this investigation. To analyze the complicated dynamics, we use a mathematical model. Subsequently, we solve these equations both analytically and numerically. The analytical method is built using the Adomian Decomposition Method (ADM), while the numerical procedure employs the Explicit Runge-Kutta Method. This study has yielded several significant findings and insights:

- Increased unsteadiness can lead to enhanced mixing and convective flow, resulting in higher velocity, temperature, and concentration profiles within certain similarity parameter ranges.
- Increased unsteadiness also makes decrease the fluid velocity that leads to momentum boundary layer thickness increase and hence the backflow phenomenon is highly favoured.
- Suction effects (negative similarity parameters) generally enhance fluid mixing and convective heat and mass transfer. Conversely, blowing effects (positive similarity parameters) may disrupt flow patterns and reduce convective heat and mass transfer rates.
- Stronger magnetic fields can enhance or diminish convective flow, depending on whether suction or blowing effects prevail. Convective heat transfer rates increase with higher Reynolds numbers, especially within laminar flow regimes.
- The stronger magnetic field has a stabilizing effect on the flow structure. As a consequence, the thickness of momentum boundary layer decreases where the reversal flow is entirely disappeared.
- Temperature and concentration profiles exhibit contrasting behaviours with changes in the similarity parameter, reflecting the interplay between suction and blowing effects.
- Suction effects generally lead to increased temperature and concentration profiles, while blowing effects may reduce them.
- Higher nanoparticle volume fractions enhance heat transfer rates by increasing the overall NF thermal conductivity and facilitating more effective heat conduction.
- According to the research unsteadiness acceleration (α = -1 to 1) causes velocity profile enhancement by 18% near the channel center given that flow fluctuations decrease the profiles by 12-15% in the vicinity of porous walls.
- The flow reversal rate decreases by 20-25% while the boundary layer stabilizes when the magnetic field strength rises from M = 1 through M = 5. At the same time, raising nanoparticle volume fractions from φ = 1 through φ = 2 boosts heat transfer rates by 8-10% because of enhanced thermal conductivity which leads to Nusselt number elevation from 0.52 to 0.57.
- For future work: Studying ideal nanoparticle concentrations/ shapes for enhanced thermal/fluid performance. The study also needs to evaluate fluid attributes such as shear-thinning behaviour together with multiple physics effects like electrothermal interactions.

Nomenclature

Symbol	Description	Units (if applicable)
A	Permeability constant	---
Br	Brinkman number	---
C	Concentration	mol/m³
Cp	Specific heat capacity	J/kg·K
D	Mass diffusivity	m²/s
Ec	Eckert number	---

f	Dimensionless velocity function	---
M	Hartmann number	---
Pr	Prandtl number	---
Re	Reynolds number	---
Sc	Schmidt number	---
T	Temperature	K
u,v	Velocity components	m/s
α	Unsteadiness parameter	---
η	Similarity variable	---
θ	Dimensionless temperature	---
μ	Dynamic viscosity	Pa·s
ρ	Density	kg/m³
σ	Electrical conductivity	S/m
φ	Dimensionless concentration	---

REFERENCES

1. Qadeer R et al. Role of nanolayer on the dynamics of tri-hybrid nanofluid subject to gyrotactic microorganisms and nanoparticles morphology vis two porous disks. Case Studies in Thermal Engineering. 2023; 51:103534.
2. Qadeer R et al. Heat and mass transfer phenomenon and aligned entropy generation with simultaneous effect for magnetized ternary nanoparticles induced by ferro and nano-layer fluid flow of porous disk subject to motile microorganisms. Numerical Heat Transfer. Part A: Applications. 2025; 86(9): 2635-2663.
3. Qadeer R et al. Significance role of dual porosity and interfacial nanolayer mechanisms on hybrid nanofluids flow: a symmetry flow model. Modern Physics Letters B. 2024; 38(08): 2450022.
4. Asgar A, Das S. Interfacial Nanolayer Aspect on Fractional Trihybrid Nanoblood Streaming in a Diverging Ciliated Micro-Vessel Under Strong Electro-Magnetism: A Renovated Hamilton-Crosser Model. Available at SSRN 4635144.
5. Mohanty D, Sivaraj R, Reddy MG, Chamkha AJ. Thermal and irreversibility analysis on Cattaneo–Christov heat flux-based unsteady hybrid nanofluid flow over a spinning sphere with interfacial nanolayer mechanism. Journal of Thermal Analysis and Calorimetry. 2023; 148(21): 12269-12284.
6. Acharya N, Sivaraj R, Panigrahi S, Jayalakshmi S. Hydrothermal variations of radiative nanofluid flow by the influence of nanoparticles diameter and nanolayer. International Communications in Heat and Mass Transfer. 2022; 130: 105781.
7. Imtiaz Ali S, Jawad M, Riaz A, Islam S. On analysis of magnetized viscous fluid flow in permeable channel with single wall carbon nanotubes dispersion by executing nano-layer approach. Alexandria Engineering Journal. 2022; 61(12): 11737-11751.
8. Sharifpur M, Yousefi S, Meyer JP. A new model for density of nanofluids including nanolayer. International Communications in Heat and Mass Transfer. 2016; 78: 168-174.
9. Abbasov HF. Determination of nanolayer thickness and effective thermal conductivity of nanofluids. Journal of Dispersion Science and Technology. 2019; 40(4): 594-603.
10. Benos LT, Sarris IE. The interfacial nanolayer role on magnetohydrodynamic natural convection of an Al_2O_3-water nanofluid. Heat Transfer Engineering. 2021; 42(2): 89-105.
11. Dawar A, Acharya N. Unsteady mixed convective radiative nanofluid flow in the stagnation point region of a revolving sphere considering the influence of nanoparticles diameter and nanolayer. Journal of the Indian Chemical Society. 2022; 99(10): 100716.
12. Muhammad R et al. Computational assesment of Carreau ternary hybrid nanofluid influenced by MHD flow for entropy generation. Journal of Magnetism and Magnetic Materials. 2023; 567: 170353.
13. Oke AS. Heat and mass transfer in 3D MHD flow of EG-based ternary hybrid nanofluid over a rotating surface. Arabian Journal for Science and Engineering. 2022; 47(12): 16015-16031.
14. Jakeer S, Reddy SRR, Rashad AM, Rupa ML, Manjula C. Nonlinear analysis of Darcy-Forchheimer flow in EMHD ternary hybrid nanofluid (Cu-CNT-Ti/water) with radiation effect. Forces in Mechanics. 2023; 10: 100177.
15. Saranya S, Duraihem FZ, Al-Mdallal QM. Quartic autocatalysis on horizontal surfaces with an asymmetric concentration: water-based ternary-hybrid nanofluid carrying titania, copper, and alumina nanoparticles. Physica Scripta. 2023; 98(7): 075214.
16. Yousef S et al. Influence of PST and PHF heating conditions on the swirl flow of Al+ Mg+ TiO_2 ternary hybrid water-ethylene glycol based nanofluid with a rotating cone. International Journal of Thermofluids. 2023; 19: 100371.
17. Sarangi MK et al. Rotational flow and thermal behavior of ternary hybrid nanomaterials at small and high Prandtl numbers. International Communications in Heat and Mass Transfer. 2022; 138: 106337.
18. Saleem N et al. Heat transport study of ternary hybrid nanofluid flow under magnetic dipole together with nonlinear thermal radiation. Applied Nanoscience. 2022; 12(9): 2777-2788.
19. Sarfraz M, Khan M. Heat transfer efficiency in planar and axisymmetric ternary hybrid nanofluid flows. Case Studies in Thermal Engineering. 2023; 44: 102857.
20. Zafar M et al. Influence of suction and heat source on MHD stagnation point flow of ternary hybrid nanofluid over convectively heated stretching/shrinking cylinder. Advances in Mechanical Engineering. 2022; 14(9): 16878132221126278.
21. Hadi Ali M et al. Numerical study on the role of ternary nanoparticles on heat transfer enhancement in MHD flow of cross-rheological-fluid. Case Studies in Thermal Engineering. 2023; 51: 103579.
22. Alnahdi AS, Nasir S, Gul T. Blood-based ternary hybrid nanofluid flow-through perforated capillary for the applications of drug delivery. Waves in Random and Complex Media. 2022; 32: 1-19.
23. Anwar S et al. Blood based hybrid nanofluid flow together with electromagnetic field and couple stresses. Scientific reports. 2021; 11(1): 12865.
24. Faisal S et al. MHD pulsatile flow of blood-based silver and gold nanoparticles between two concentric cylinders. Symmetry. 2022; 14(11): 2254.
25. Alhussain ZA, Tassaddiq A. Thin film blood based Casson hybrid nanofluid flow with variable viscosity. Arabian journal for science and Engineering. 2022; 47(1): 1087-1094.
26. Waqas H, Khan SA, Muhammad T. Thermal analysis of magnetized flow of AA7072-AA7075/blood-based hybrid nanofluids in a rotating channel. Alexandria Engineering Journal. 2022; 61(4): 3059-3068.
27. Abas SA, Ullah H, Islam S, Fiza M. A passive control of magnetohydrodynamic flow of a blood-based Casson hybrid nanofluid over a convectively heated bi-directional stretching surface. ZAMM-Journal of Applied Mathematics and Mechanics/Zeitschrift für Angewandte Mathematik und Mechanik. 2024; 104(1): e202200576.
28. Ashraf MU, Qasim M, Wakif A, Afridi MI, Animasaun IL. A generalized differential quadrature algorithm for simulating magnetohydrodynamic peristaltic flow of blood-based nanofluid containing magnetite nanoparticles: a physiological application. Numerical Methods for Partial Differential Equations. 2022; 38(3): 666-692.
29. Dolui S, Bhaumik B, De S, Changdar S. Effect of a variable magnetic field on peristaltic slip flow of blood-based hybrid nanofluid through a nonuniform annular channel. Journal of Mechanics in Medicine and Biology. 2023; 23(1): 2250070.
30. Rajkumar D, Reddy AS, Narayana PS, Jagadeshkumar K, Chamkha AJ. Pulsating magnetohydrodynamic flow of Fe3O4-blood based micropolar nanofluid between two vertical porous walls with Cattaneo–Christov heat flux and entropy generation. Journal of Magnetism and Magnetic Materials. 2023; 571: 170564.
31. Nilankush A. Magnetically driven MWCNT-Fe3O4-water hybrid nanofluidic transport through a micro-wavy channel: a novel MEMS

design for drug delivery application. Materials Today Communications. 2024; 38: 107844.
32. Nilankush A. Hydrothermal scenario of buoyancy-driven magnetized multi-walled carbon nanotube-Fe3O4-water hybrid nanofluid flow within a discretely heated circular chamber fitted with fins. Journal of Magnetism and Magnetic Materials. 2024; 589: 171612.
33. Nilankush A. Magnetized hybrid nanofluid flow within a cube fitted with circular cylinder and its different thermal boundary conditions. Journal of Magnetism and Magnetic Materials. 2022; 564: 170167.
34. Nilankush A. On the hydrothermal behavior and entropy analysis of buoyancy driven magnetohydrodynamic hybrid nanofluid flow within an octagonal enclosure fitted with fins: Application to thermal energy storage. Journal of Energy Storage. 2022; 53: 105198.
35. Sihem G et al. Insight into the dynamics of slip and radiative effect on magnetohydrodynamic flow of hybrid ferroparticles over a porous deformable sheet. ZAMM-Journal of Applied Mathematics and Mechanics/Zeitschrift für Angewandte Mathematik und Mechanik. 2024; 104(4): e202300729.
36. Samina N et al. Modeling of EMHD ternary hybrid Williamson nanofluid flow over a stretching sheet with temperature jump and magnetic induction. Numerical Heat Transfer, Part B: Fundamentals. 2024; 1-15.
37. Mohamed K et al. Velocity slip and temperature jump effects on entropy generation of MHD second-grade hybrid nanofluid in Jeffery-Hamel flow. International Journal of Numerical Methods for Heat & Fluid Flow. 2024; 34(10): 3637-3658.
38. Ameur G et al. Irreversibility of Al_2O_3-Ag hybrid nanoparticles in mixture base fluid on microchannel with variable viscosity, buoyancy forces, and suction/injection effects: an analytical study. International Journal of Heat and Fluid Flow. 2024; 107: 109341.
39. Mohamed K et al. Magneto hydrodynamic boundary layer flow of ternary hybrid nano-fluid (TiO_2-SiO_2,-Al_2O_3/H_2O-$C_2H_6O_2$) a numerical and analytical Investigations. Journal of the Brazilian Society of Mechanical Sciences and Engineering. 2024; 46(6): 378.
40. Mohamed K et al. Duan Rach approach solution of MHD flow of ternary hybrid Casson magnetized nanofluid in converging/diverging geometry with velocity slip effects. Numerical Heat Transfer, Part A: Applications. 2024; 1-18.
41. Mehdi O et al. Heat transfer characteristics of moving longitudinal porous fin wetted with ternary (Cu–Al_2O_3–TiO_2) hybrid nanofluid: ADM solution. The European Physical Journal Plus. 2023; 138(9): 1-12.
42. Jawad M, Saeed A, Gul T, Khan A. The magnetohydrodynamic flow of a nanofluid over a curved exponentially stretching surface. Heat Transfer. 2021; 50(6): 5356-5379.
43. Farhan A et al. Numerical scrutinization of Darcy–Forchheimer flow for trihybrid nanofluid comprising of GO+ ZrO_2+ SiO_2/kerosene oil over the curved surface. Journal of Thermal Analysis and Calorimetry. 2025; 150(4): 2667-2682.
44. Arshad K et al. Thermal examination for double diffusive MHD Jeffrey fluid flow through the space of disc and cone apparatus subject to impact of multiple rotations. International Journal of Heat and Fluid Flow. 2024; 106: 109295.
45. Ali A, Das S. Applications of neuro-computing and fractional calculus to blood streaming conveying modified trihybrid nanoparticles with interfacial nanolayer aspect inside a diseased ciliated artery under electroosmotic and Lorentz forces. International Communications in Heat and Mass Transfer. 2024; 152: 107313.
46. Ali A, Das S, Muhammad T. Dynamics of blood conveying copper, gold, and titania nanoparticles through the diverging/converging ciliary micro-vessel: further analysis of ternary-hybrid nanofluid. Journal of Molecular Liquids. 2023; 390: 122959.
47. Ali A, Das S. Electroosmotic influence on fractional Jeffrey blood flow with nanolayer-coated tetra-hybrid nanoparticles in an electrified stenotic-aneurysm artery. Computers in Biology and Medicine. 2025; 188: 109819.
48. Dolui S, Bhaumik B, De S. Combined effect of induced magnetic field and thermal radiation on ternary hybrid nanofluid flow through an inclined catheterized artery with multiple stenosis. Chemical Physics Letters. 2023; 811: 140209.
49. Dolui S, Bhaumik B, De S, Changdar S. Biomedical simulations of hybrid nano fluid flow through a balloon catheterized stenotic artery with the effects of an inclined magnetic field and variable thermal conductivity. Chemical Physics Letters. 2023; 829: 140756.
50. Majdalani J, Zhou C, Dawson CA. Two-dimensional viscous flow between slowly expanding or contracting walls with weak permeability. Journal of Biomechanics. 2002; 35(10): 1399-1403.
51. Qureshi MZA, Ali K, Iqbal MF, Ashraf M, Ahmad S. Heat and mass transfer enhancement of nanofluids flow in the presence of metallic/metallic-oxides spherical nanoparticles. The European Physical Journal Plus. 2017; 132(1): 57.

Ibrahim Mahariq: https://orcid.org/0000-0002-7222-3014

Mohamed Kezzar: https://orcid.org/0000-0003-2042-7696

Pachiyappan Ragupathi: https://orcid.org/0000-0003-4713-9352

Umair Khan: https://orcid.org/0000-0002-2034-1211

Farhan Lafta Rashid: https://orcid.org/0000-0002-7609-6585

Abeer Shaaban: https://orcid.org/0000-0001-5784-8705

Mohamed Rafik Sari: https://orcid.org/0000-0002-8636-8863

Appendix A

The process transforms a nonlinear boundary value problem into a first order initial value problem by introducing new variables $\mathcal{Y}_1(\eta)$, $\mathcal{Y}_2(\eta)$, $\mathcal{Y}_3(\eta)$, $\mathcal{Y}_4(\eta)$ and $\mathcal{Y}_5(\eta)$. Eqs (9-11) with the associated boundary conditions Eq (12), can then be expressed in the following form using these variables:

Tab. A. 1. The solution procedure based on the ERKM

Equations	Conditions
$\mathcal{Y}_1' = \mathcal{Y}_2$	$\mathcal{Y}_1(-1) = -1$
$\mathcal{Y}_2' = \mathcal{Y}_3$	$\mathcal{Y}_2(-1) = 0$
$\mathcal{Y}_3' = \mathcal{Y}_4$	$\mathcal{Y}_3(-1) = \alpha_1$
$\mathcal{Y}_4' = \frac{A_2}{A_1}\langle +\alpha(3\mathcal{Y}_3 + \eta\mathcal{Y}_3') + Re(\mathcal{Y}_2\mathcal{Y}_3 - \mathcal{Y}_1\mathcal{Y}_3') + {A_2}^{-1}A_3M\mathcal{Y}_3\rangle$	$\mathcal{Y}_4(-1) = \alpha_2$
$\mathcal{Y}_5' = \mathcal{Y}_6$	$\mathcal{Y}_5(-1) = 1$
$\mathcal{Y}_6' = \frac{1}{A_4}\langle +A_5Pr\mathcal{Y}_6(\eta_\alpha - \mathcal{Y}_1Re) + A_1Br\,Re^2{\mathcal{Y}_3}^2\rangle$	$\mathcal{Y}_6(-1) = \alpha_3$
$\mathcal{Y}_7' = \mathcal{Y}_8$	$\mathcal{Y}_7(-1) = 1$
$\mathcal{Y}_7' = \langle +Sc\,\mathcal{Y}_8(\eta\alpha - \mathcal{Y}_1\,Re) - K_r\mathcal{Y}_7\rangle$	$\mathcal{Y}_8(0) = \alpha_4$

The compared are approximated using HAM-based Mathematica package and with the ones reported in existing literature.

$$\frac{A_1}{A_2}f'''' + \alpha(3f'' + \eta f''') + Re(f'f'' - ff''') + {A_2}^{-1}A_3Mf'' = 0$$

In ADM method Eq. (9) can be written

$$\mathcal{L}f'''' = \frac{A_1}{A_2}\langle +\alpha(3f'' + \eta f''') + Re(f'f'' - ff''') + {A_2}^{-1}A_3Mf''\rangle. \tag{A.1}$$

Here the operator of differential $\mathcal{L}$ and the operator of inverse $\mathcal{L}^{-1}$ are presented respectively by

$$\mathcal{L}_f = \frac{d^4}{d\eta^4},$$

$$\mathcal{L}_f{}^{-1}(\blacksquare) = \int_0^\eta\int_0^\eta\int_0^\eta\int_0^\eta(\blacksquare)\,d\eta d\eta d\eta d\eta \tag{A.2}$$

After applying boundary constraints and operating with $\mathcal{L}^{-1}$ on Eq. (A.1), we get

$$f = f(-1) + f'(-1)\eta + f''(-1)\frac{\eta^2}{2} + f'''(-1)\frac{\eta^3}{6} +$$
$$\int_0^\eta\int_0^\eta\int_0^\eta\int_0^\eta\frac{A_2}{A_1}\langle +\alpha(3f'' + \eta f''') + Re(f'f'' - ff''') + {A_2}^{-1}A_3Mf''\rangle\,d\eta d\eta d\eta d\eta \tag{A.3}$$

$$f = f(-1) + f'(-1)\eta + f''(-1)\frac{\eta^2}{2} + f'''(-1)\frac{\eta^3}{6}$$

However, when the boundary conditions (12) are taken into consideration, the equation (A.3) changes to:

$$f(\eta) = -1 + a\frac{\eta^2}{2} + b\frac{\eta^3}{6} + \int_0^\eta\int_0^\eta\int_0^\eta\int_0^\eta\frac{A_2}{A_1}\langle +\alpha(3f'' + \eta f''') + Re(f'f'' - ff''') + {A_2}^{-1}A_3Mf''\rangle\,d\eta d\eta d\eta d\eta \tag{A.4}$$

Lastly, the following are the elements of the solution that the ADM algorithm produced

$$f(\eta) = f_0 + \int_0^\eta\int_0^\eta\int_0^\eta\int_0^\eta\frac{A_2}{A_1}\langle +\alpha(3f'' + \eta f''') + Re(f'f'' - ff''') + {A_2}^{-1}A_3Mf''\rangle\,d\eta d\eta d\eta d\eta \tag{A.5}$$

where

$$f_0 = -1 + a\frac{\eta^2}{2} + b\frac{\eta^3}{6} \tag{A.6}$$